

See discussions, stats, and author profiles for this publication at: <https://www.researchgate.net/publication/236641261>

# Solvothermal One-Step Synthesis of Ni-Al Layered Double Hydroxide/Carbon Nanotube/Reduced Graphene Oxide Sheet Ternary Nanocomposite with Ultrahigh Capacitance for Supercapacitors

ARTICLE in ACS APPLIED MATERIALS & INTERFACES · MAY 2013

Impact Factor: 6.72 · DOI: 10.1021/am4003843 · Source: PubMed

---

CITATIONS

50

---

READS

98

6 AUTHORS, INCLUDING:



Zan Gao

University of Virginia

33 PUBLICATIONS 1,351 CITATIONS

SEE PROFILE



Milin Zhang

Harbin Engineering University

182 PUBLICATIONS 4,748 CITATIONS

SEE PROFILE

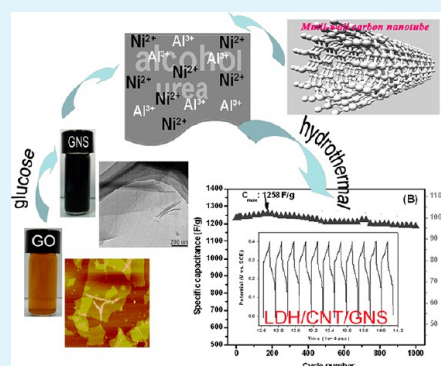
# Solvothermal One-Step Synthesis of Ni–Al Layered Double Hydroxide/Carbon Nanotube/Reduced Graphene Oxide Sheet Ternary Nanocomposite with Ultrahigh Capacitance for Supercapacitors

Wanlu Yang,<sup>†</sup> Zan Gao,<sup>†</sup> Jun Wang,<sup>\*,†,‡</sup> Jing Ma,<sup>†</sup> Milin Zhang,<sup>†,‡</sup> and Lianhe Liu<sup>†,‡</sup>

<sup>†</sup>Key Laboratory of Superlight Material and Surface Technology, Ministry of Education, and <sup>‡</sup>Institute of Advanced Marine Materials, Harbin Engineering University, Harbin 150001, People's Republic of China

**ABSTRACT:** A Ni–Al layered double hydroxide (LDH), multi-wall carbon nanotube (CNT), and reduced graphene oxide sheet (GNS) ternary nanocomposite electrode material has been developed by a facile one-step ethanol solvothermal method. The obtained LDH/CNT/GNS composite displayed a three-dimensional (3D) architecture with flowerlike Ni–Al LDH/CNT nanocrystallites gradually self-assembled on GNS nanosheets. GNS was used as building blocks to construct 3D nanostructure, and the LDH/CNT nanoflowers in turn separated the two-dimensional (2D) GNS sheets, which preserved the high surface area of GNSs. Furthermore, the generated porous networks with a narrow pore size distribution in the LDH/CNT/GNS composite were also demonstrated by the N<sub>2</sub> adsorption/desorption experiment. Such morphology would be favorable to improve the mass transfer and electrochemical action of the electrode. As supercapacitor electrode material, the LDH/CNT/GNS hybrid exhibited excellent electrochemical performance, including ultrahigh specific capacitance (1562 F/g at 5 mA/cm<sup>2</sup>), excellent rate capability, and long-term cycling performance, which could be a promising energy storage/conversion material for supercapacitor application.

**KEYWORDS:** layered double hydroxides, carbon tube, graphene nanosheet, ternary composite, supercapacitor, electrochemical property



## 1. INTRODUCTION

With the worsening fossil energy depletion and global warming, there is an urgent need for efficient, clean and sustainable sources of energy, as well as new energy storage devices with high energy densities and power densities. Supercapacitors (SCs, also known as electrochemical capacitors or ultracapacitors), with higher energy densities and greater power densities compared to conventional capacitors, and longer cycle life than secondary batteries, seem to be the most possible candidate to meet the future energy requirement.<sup>1–4</sup> Electrode materials are one of the most important factors to determine the performance of SCs. In general, based on the charge/discharge mechanisms, electrode materials for SCs could be classified into two types: electrical double layer capacitance materials (EDLC, mainly are carbon materials) and pseudocapacitance materials (including conducting polymers, metal oxides or hydroxides etc.).<sup>1</sup> Both EDLC and pseudocapacitance include surface phenomena depending on their surface area. Therefore, electrode materials with suitable porous structure and larger surface areas are beneficial for the higher capacitance, which may facilitate the electron transport and shorten the transmission distance. So the commonly used electrode materials are nanoscaled materials with larger porosity and higher specific surface area.

To date, different carbon materials (such as active carbon, carbon tubes, carbon fibers, and graphene sheets), due to their

low cost, environmental friendliness, high flexibility and conductivity, stable mechanical strength, have been realized as the most preferable materials for SC electrodes.<sup>5</sup> Graphene, as single-layer planar sheets with sp<sup>2</sup>-bonded carbon atoms densely packed in a honeycomb crystal lattice, is a rising star in the carbon family.<sup>6</sup> As the origin of all graphitic forms, graphene sheet could roll up into 1D carbon nanotube (CNT), and also has many similarities to CNT in structure and property, such as high aspect ratio, rich electronic states, large surface area, and good mechanical properties.<sup>7</sup> As shining stars in energy storage applications, single-walled carbon nanotubes (SWCNT), multiwalled carbon nanotubes (MWCNT), and GNS have shown excellent EDLC performances.<sup>8,9</sup> In theory, the specific surface area of the isolated GNS sheets is ~2600 m<sup>2</sup>/g and the capacitance can achieve 550 F/g. But the restacking and agglomeration of GNS sheets results from the strong van der Waals interaction among the neighboring layers leads to the obvious reduction both of the surface area of GNS and the accessibility of the electrolyte. In the past few years, many works focused on combining metal oxides or conducting polymers with GNS to form GNS-based hybrid materials, using these pseudocapacitance materials as spacers materials to

**Received:** January 29, 2013

**Accepted:** May 6, 2013

**Published:** May 6, 2013

separate the adjacent graphene sheets.<sup>10–12</sup> Similarly, other carbon materials (activated carbon, CNTs etc.) could also be applied as spacers for the same purpose to form hybrid electrode.<sup>13,14</sup> For example, some efforts have been made to prepare GNS/CNT composite films, such as layer-by-layer electrostatic self-assembly, chemical vapor deposition, in situ growth, and spin-coating homogeneously mixed solutions of the two components.<sup>13,15–17</sup> Nevertheless, the GNS/CNT binary composites still show the relative low specific capacitance (120–160 F/g), presumably due to the limited accessible surface area for electrolyte ions. In further studies, to improve the specific capacity of the GNS/CNT hybrid, high capacitive  $\text{MnO}_2$  was coated on CNTs and then combined with GNS to form  $\text{MnO}_2$ -coated CNTs/GNS composite. And the maximum capacitance obtained for the ternary composite electrode was 193 F/g.<sup>18</sup>

Layered double hydroxides (LDHs), also known as hydro-talcite-like materials or anionic clays, are a family of layered solids with structurally positively charged layers and interlayer balancing anions.<sup>19,20</sup> Because of the tunable composition and flexible ion-exchangeability, LDHs have a large number of important applications in catalysis, sensors, drug/gene delivery and matrix materials in hybrid composites, etc.<sup>21–24</sup> In electrochemical field, LDHs are promising for the next-generation SCs, in which EDLC and pseudocapacitance could be simultaneously acquired due to their abundant electrochemically active sites and slabs.<sup>25</sup> However, the relative low mass diffusion and electron transfer of LDHs constrain the high-rate charge/discharge capability and therefore impact the performance of electrode materials. Hence, a composite electrode material with LDH anchored on a conductive substrate with high surface area is thought to be an ideal method to improve the electrochemical property. Malak-Polaczyk et al. reported a simple chemical precipitation to fabricate LDHs/activated carbon composite electrodes for supercapacitor, which exhibited an excellent performance for energy storage, and 15% loss of the capacitance was observed after 15 000 cycles.<sup>26</sup> Wang et al. adopted an innovative strategy to fabricate electrode materials by layered assembling single layer graphene oxide (GO) sheets and Co–Al LDH nanosheets. The maximum specific capacitance of this composite was calculated to be 1031 F/g and there was no obvious decrease of specific capacitance at the current density of 20 A/g after 6000 cycles.<sup>27</sup> Up to now, various carbon/LDHs composites (CNT/LDH, graphene oxide/LDH) have exhibited improved pseudocapacitor performance.<sup>2,28–30</sup> Despite the great progresses have been achieved, a huge challenge for LDH-based composites still remains to realize the high specific capacitance, outstanding rate performance and long-lasting property simultaneously. Besides, many of the applications of LDH in SCs are still largely restricted because of the inaccessibility for electrolyte ions to the inner surfaces of the LDH layers. At present, a focus for LDH researches is to fabricate well-defined micro/meso-structures with higher surface areas and narrow pore-size distribution to maximize the utility of LDH layers.<sup>29</sup>

We have previously reported a novel hybrid GNS/LDH material by in situ growth hexagonal LDHs on GNS nanosheets for the first time, which proposed a new direction of the LDH-based composite materials for SC applications.<sup>31</sup> More recently, Chen et al. and Dong et al. reported that GO and Co–Al LDH could also be layer-by-layer assembled with polyelectrolyte (PVA and PDDA) based on hydrogen-bonding interaction and

electrostatic attraction, respectively.<sup>32,33</sup> By this way, the agglomeration of LDH layers produced from the high charge density during the fabrication process was also avoided. However, more facile and effective routes are still highly required to exploit LDH-based composites and improve their energy storage performance.

On the basis of the previous work, we studied the synthesis procedure and capacitive behaviors of a 3D ordered GNS-based architecture composed of Ni–Al LDH/CNT nanoflowers and GNS nanosheets in this paper. Unlike the usual hexagonal platelets morphology, a flowerlike hierarchical Ni–Al LDH structure with lots of mesopores formed by controlling the preparation conditions, without any complicated intercalation procedure or the specialized templates. In the resultant LDH/CNT/GNS composite, CNTs grew along the Ni–Al LDH platelets as the building blocks to construct flowerlike LDH/CNT nanoparticles, and the formed LDH/CNT particles uniformly incorporated into the GNS sheets to form an open 3D conductive network. To the best of our knowledge, there are rarely reports about combining 3D LDH nanostructure with carbon materials to prepare ternary composite. Furthermore, the high specific surface areas and pore networks of the LDH/CNT/GNS composite may be beneficial for the improvement of the electrochemical property. The composite electrode exhibited a maximal capacitance of 1869 F/g (at the current density of 1 mA/cm<sup>2</sup>), good rate capability (with the residual capacitance of 713.4 F/g at the high current density of 100 mA/cm<sup>2</sup>), and excellent cycle life with only 3.5% deterioration of the initial specific capacity after 1000 cycle tests, which can be potentially used in energy storage/conversion devices.

## 2. EXPERIMENTAL SECTION

**2.1. Material Synthesis. Synthesis of Ni–Al LDHs.** Porous Ni–Al LDHs were synthesized by a facile ethanol solvothermal method as our previous work.<sup>34</sup> Briefly, 0.003 mol of  $\text{Al}(\text{NO}_3)_3 \cdot 9\text{H}_2\text{O}$  and 0.009 mol of  $\text{Ni}(\text{NO}_3)_2 \cdot 6\text{H}_2\text{O}$  were dissolved in a 80 mL of ethanol solution containing 0.04 mol urea. After magnetically stirring for 60 min at room temperature, the above solution was then transferred to a sealed autoclave, and heated at 140 °C for different time (6–14 h). The autoclave was then naturally cooled down to room temperature. The obtained green product was washed several times with water and ethanol, and then dried at 60 °C for 8 h to obtain the final product.

**Synthesis of LDH/CNT/GNS Composite.** Glucose was used as a green reductant reducing agent to prepare GNS sheets from graphite oxide (GO).<sup>35</sup> And the GO was synthesized from natural graphite by a modified Hummers method.<sup>36</sup> Commercial multiwall CNTs with diameter of 20–50 nm (Shenzhen Nanotech Port Co. Ltd.) were purified by refluxing the sample in 30 wt % nitric acid for 12 h. Then the acid-treated CNTs were collected by vacuum filtration and dried at 60 °C for 12 h. GNSs (0.05 g) and CNTs (0.05 g) were subjected to ultrasonic dispersion in ethanol for 1 h to form uniform suspension. Then the above  $\text{Ni}(\text{NO}_3)_2$ ,  $\text{Al}(\text{NO}_3)_3$  and urea was mixed with the carbon suspension to form a 80 mL solution, and treated it with ultrasonic vibration. Finally, the solvothermal reaction was carried out at 140 °C for 14 h. The mass ratio of LDH/CNT/GNS composite was controlled by the feeding amounts of GNS and CNT. The amount of LDH was obtained by reduction of the mass of GNS and CNT in the final composite. We consider the mass of the carbon materials in the reaction process is constant. The final mass ration of the LDH, CNT, and GNS in the composite was 90:5:5. For comparison, LDH/GNS and LDH/CNT binary composites with the same total carbon content as LDH/CNT/GNS have also been synthesized by the same way without the introduction of CNTs or GNSs, respectively.

**2.2. Characterization.** The microstructures of the materials were investigated by scanning electron microscopy (SEM) (JEOL JSM-6480A microscope) and transmission electron microscopy (TEM)



(Philips CM 200 FEG, 160 kV). The crystallographic structures of the samples were determined by a X-ray diffraction system (XRD) (Rigaku TTR-III) equipped with Cu K $\alpha$  radiation ( $\lambda = 0.15406$  nm). Fourier transform infrared spectra (FT-IR) of the samples were recorded in the range 4000–400  $\text{cm}^{-1}$  with 2  $\text{cm}^{-1}$  resolution using the KBr pellet technique on a Bruker Vector-22 Fourier transform spectrometer. Raman measurements were performed by a Jobin Yvon HR800 micro-Raman spectrometer at 457.9 nm. The laser beam was focused with a 50X objective lens to about 1  $\mu\text{m}$  spot on the surface of the sample. X-ray photoelectron spectroscopy (XPS) measurements were carried out by a PHI 5700 ESCA spectrometer with monochromated Al K $\alpha$  radiation ( $h\nu = 1486.6$  eV). All the XPS spectra were corrected by the C 1s line at 284.5 eV. Surface area measurements were performed by the physical adsorption of  $\text{N}_2$  at 77 K (Micromeritics ASAP 2010) and obtained by the Brunauer–Emmett–Teller method (BET).

**2.3. Electrochemical Performance Test.** The electrochemical performances of as-obtained products were investigated by a three-electrode test system using a CHI 660D electrochemical workstation. The working electrodes were fabricated by a reported procedure.<sup>37</sup> Briefly, the as-prepared samples, acetylene black, and polytetrafluoroethylene (PTFE) with a weight of about 20 mg were mixed in a mass ratio of 80:15:5 and then was dispersed by ethanol to produce a homogeneous paste. Acetylene black and PTFE were used as the conductive agent and binder, respectively. The resulting paste was then coated onto the nickel foam (1  $\text{cm} \times 1$  cm) to fabricate the working electrode. The total amount of the active materials coated onto the electrode is about 16  $\text{mg}/\text{cm}^2$ . Platinum foil (2  $\text{cm} \times 2$  cm) and a saturated calomel electrode (SCE) were used as the counter and reference electrodes, respectively. The electrochemical measurements were performed in a 6 M KOH electrolyte at the room temperature. CV tests were carried out between 0 and 0.6 V (vs SCE) at the scan rates of 5, 10, 20, 50 mV/s. Galvanostatic charge/discharge tests were performed in the potential range of 0 to 0.42 V (vs SCE) at the different current densities. The EIS data were collected with the frequency range of 0.05 Hz to 100 kHz with the AC voltage amplitude of 5 mV.

### 3. RESULTS AND DISCUSSION

**3.1. Morphology and Structure.** As in the previous work,<sup>34</sup> Ni–Al LDH was first carried out at 140  $^{\circ}\text{C}$  for different aging times of 6, 10, and 14 h under an ethanol solvothermal condition. SEM and TEM were used to investigate the time-dependent evolution of morphology of the pristine Ni–Al LDHs crystals (Figure 1). Large numbers of LDH sheets with an average size of several hundreds of nanometers and a nanoscale thickness are formed after aging 6 h (Figure 1a). The TEM image (Figure 1d) reveals that the LDH sheets are hexagonal platelet-like morphology with irregular edges. Images

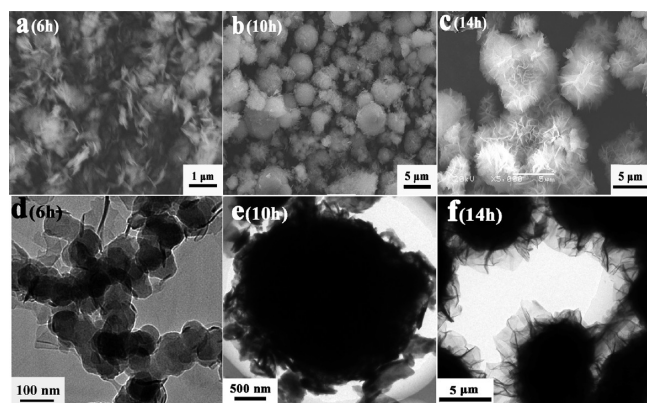


**Figure 1.** Morphology changes of pristine Ni–Al LDH with reaction time under ethanol solvent thermal condition.

b and e in Figure 1 correspond to the morphology of the sample collected after 10 h aging time at 140  $^{\circ}\text{C}$ , which shows the coexistence of LDH sheets and a large number of microspheres with rough surfaces, which is caused by the irregular superposition of LDH sheets. When the aging time is prolonged to 14 h, no separate LDH sheets remained and the sample entirely became the flowerlike hierarchical porous microspheres with the particle size of several micrometers, as shown in images c and f in Figure 1. The surfaces of the microspheres are composed of ultrathin secondary LDH sheets with about 1–3  $\mu\text{m}$  in length, which are assembled by lots of smaller primary LDH platelets. Unlike the product collected at 10 h, the outer surfaces of these microspheres include many flexible nanosheets which wrap and connect with each other. Those nanosheets protend from the center of microsphere and uniformly distribute in all directions. Moreover, the increase in average diameters of those LDH microspheres reveals that the hierarchical porous microspheres are assembled from the spherical aggregates at the earlier stage ( $\sim 10$  h). The morphology of this flowerlike LDH nanostructure is much different from the conventional 2D hexagonal shape. And the mesoporous structure inside the LDH microspheres could also facilitate the improvement of the pseudocapacitance property.

The preparation condition of the flowerlike LDH nanostructure was chosen to investigate the impact of GNS and CNT on the morphology of LDH. Because of the addition of GNSs into the reaction system, the process of LDH sheets self-assembled into flowerlike microsphere has been changed. As seen in images a and b in Figure 2, unlike the usual bulk aggregates of GNS sheets, LDH/GNS binary composite exhibits a loose lamellar nanostructure, with Ni–Al LDH nanosheets vertical distributing on the surfaces of GNS sheets or inserting into the interlayer of GNS sheets. The restacking of GNS sheets and the aggregation of layered LDHs were effectively avoided, which also prevents the loss of the active surface areas of both GNS and LDH. Comparing with the traditional face-to-face assembling, the ultrathin LDH platelets grew vertically and cross-linked on the GNS substrate, which provides a porous structure in the LDH/GNS composite, enabling much higher specific surface area and more efficient penetration of electrolytes into electrodes. The TEM image in Figure 2c also demonstrates the upright growth of LDH platelets on the surfaces of completely exfoliated GNS sheets with scrolled and corrugated morphology. The perfect combination of the two platelet-like components was not achieved in the previous researches.<sup>31,32,38</sup> Figure 2d displays the SEM image of the LDH/CNT binary composite obtained under the same condition, which illustrate a well-dispersed and spherelike morphology with the particle size of several micrometers. The flowerlike LDH/CNT microspheres are composed of numerous LDH nanosheets and CNTs intercrossed with each other. And the size of the LDH/CNT microsphere is obviously smaller than that of pristine LDH microspheres and there are no obvious aggregates, which make for the improvement of effective area for charge accumulation. The tight combination between CNTs and LDH platelets could also be obviously observed in Figure 2f, individual CNTs are randomly dispersed on the surfaces of LDH platelets and inside the microspheres, and no aggregation is observed. These results further indicate the strong interaction among CNTs and LDHs, which prevents the agglomeration of LDHs. Furthermore, a partly hollow structure appeared in LDH/CNT composite, through which the active material inside the microspheres could also be fully

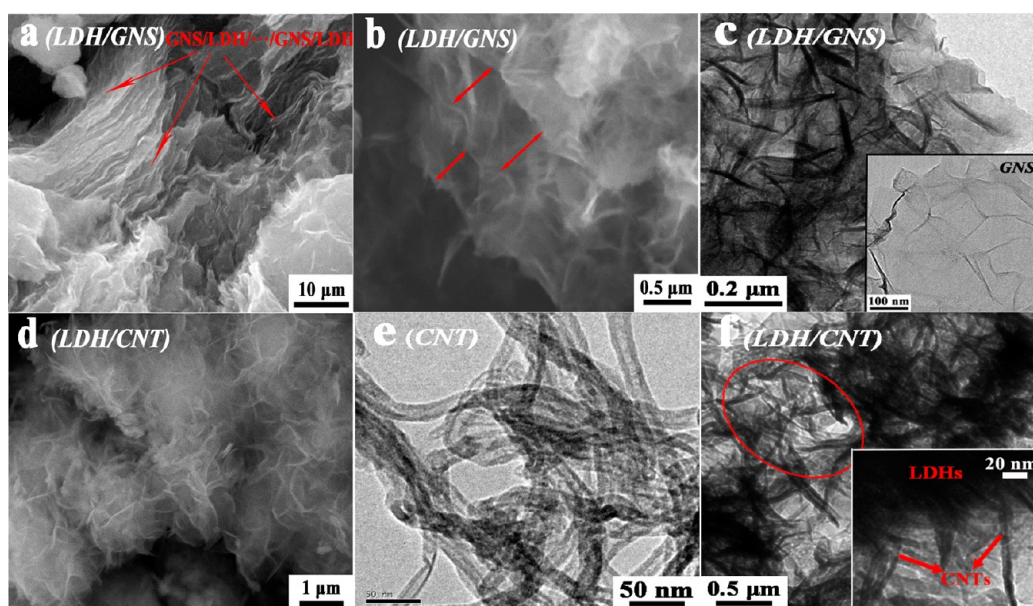


**Figure 2.** SEM and TEM images of (a–c) LDH/GNS and (d, f) LDH/CNT binary composites, with the morphology of upright LDH platelets anchored on GNS sheets and flowerlike microsphere, respectively; (e) TEM image of pristine acid-treated CNTs.

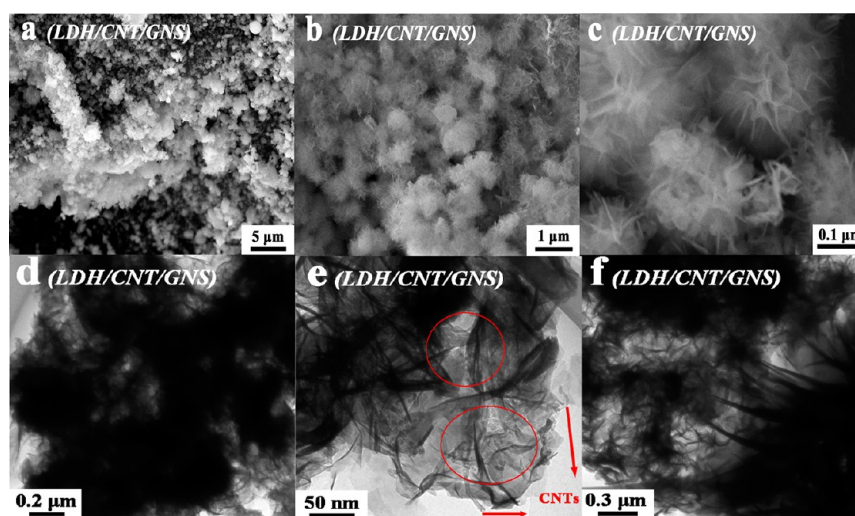


**Figure 3.** (a–c) SEM and (d–f) TEM images of LDH/CNT/GNS composite at different magnification levels.

used. For the purpose of more effective combining, the CNT used here was acid modified, so a relatively rough surface is observed in the TEM image of pure CNTs (Figure 2e). On the other hand, curved morphology of LDHs in the two binary composites implies that the addition of GNS or CNT play an important role in forming the curved sheetlike LDH nanocrystals.

A well-defined microstructure with higher surface area and pore-size distribution of LDH-based composite could guarantee all the electroactive components take part in the redox reactions and promise a fast electron and mass transfer in SCs.<sup>39</sup> GNS sheets separated by LDH/CNT nanoparticles could be observed in the LDH/CNT/GNS ternary composite as shown in Figure 3. In the LDH/CNT/GNS composite, a large number of flowerlike LDH/CNT nanospheres dispersed on the lamellar surfaces and the edges of the GNS sheets, with smaller average diameters of 200–500 nm than that of pristine LDH/CNT binary composite. At higher magnification (Figure

3c, e), it can be seen that such assembled LDH/CNT spheres are formed by many curved and intercrossed LDH sheets with some CNTs randomly distributed on their surfaces as indicated by the red arrows, indicating the same assembly process of flowerlike LDH/CNT in the ternary and binary composites. In images d and f in Figure 3, a large amount of LDH/CNT nanospheres disperse on the surfaces of GNS sheets to form a porous nanostructure, and no aggregation is observed. The strong interaction between LDHs, CNTs, and GNSs prevents formation of agglomerates and the LDH/CNT nanoflowers result in the exfoliation of GNS sheets, which consists with the following XRD results (Figure 4A g). Meanwhile, the open framework of LDH/CNT/GNS may provide lots of highly exposed electrochemically active sites, which could lead to the full utilization of electrochemical active materials and provide a higher specific capacitance.

The X-ray diffraction (XRD) patterns recorded for all samples are shown in Figure 4A. The XRD pattern of the acid-

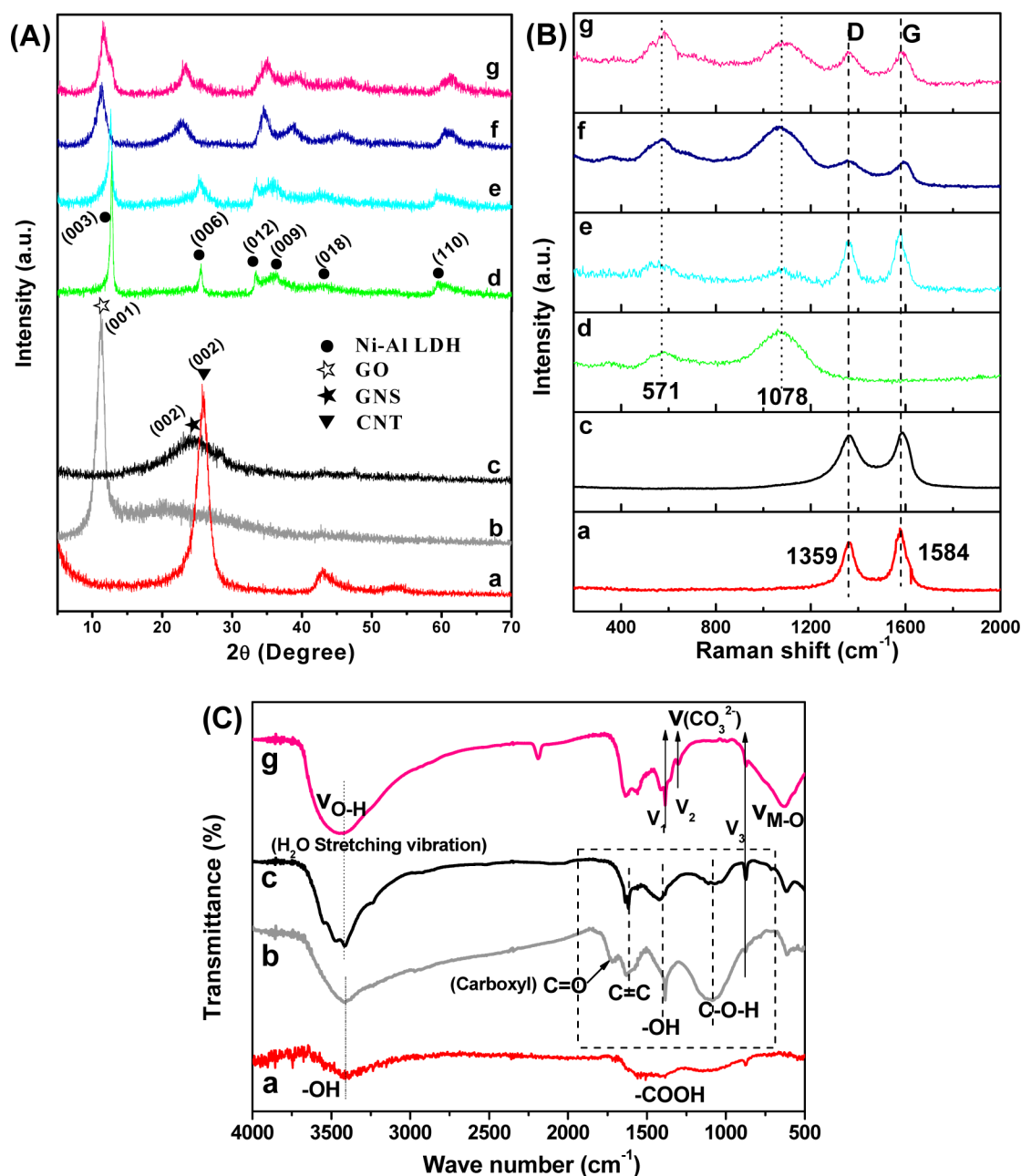


**Figure 4.** (A) XRD patterns, (B) Raman spectra, and (C) FT-IR spectra for (a) acid-treated CNT, (b) GO, (c) GNS, (d) Ni-Al LDH, (e) LDH/CNT, (f) LDH/GNS, and (g) LDH/CNT/GNS.

treated CNT (CNT-COOH) shows three diffraction peaks at 26.5, 43.2, and 54.2° which are indexed as the (002), (100) and (004) plane of layered and hexagonal graphene structure of CNTs (Figure 4A a).<sup>40</sup> The feature diffraction peak of exfoliated graphite oxide (GO) at about 10.8° (001) with a basal spacing of 0.82 nm, indicating the graphite was totally exfoliated to GO and oxygen-containing functional groups was also introduced to the graphite sheets (Figure 4A b).<sup>41</sup> After the reduction of glucose, most of the oxygen-containing groups on GO are removed, at the same time, a broad diffraction peak (002) appeared at about 24.5°, which indicates the great reduction of GO to layered GNS (Figure 4A c).<sup>42,43</sup> Additionally, the *d*-spacing of GO (0.82 nm) is changed to 0.37 nm of GNS, which is still a little larger than that of natural graphite (0.34 nm), evincing the incomplete reduction of GO

to GNS and the residual oxygen-containing groups and hydrogen on GNS sheets.<sup>10</sup>

For the XRD patterns of pristine LDH and LDH-carbon composites, characteristic reflections peaks of LDH materials with a series of (001) peaks at low angle are observed, all the diffraction peaks could be indexed to a typical rhombohedral phase Ni-Al hydroxalite (JCPDS No. 15-0087). The sharp diffraction peaks in Figure 4A d reveal the highly crystallinity and excellent layered feature of the pristine Ni-Al LDH. The *d*-spacing (0.693 nm) of (003) reflection peak of LDH sample in the solvothermal condition is smaller than that of LDHs prepared in hydrothermal condition (typically larger than 0.75 nm),<sup>38,44,45</sup> which indicates a lower content of intercalated H<sub>2</sub>O and CO<sub>3</sub><sup>2-</sup> caused by the 100% ethanol solvothermal conditions. No typical diffraction peaks of CNTs are observed



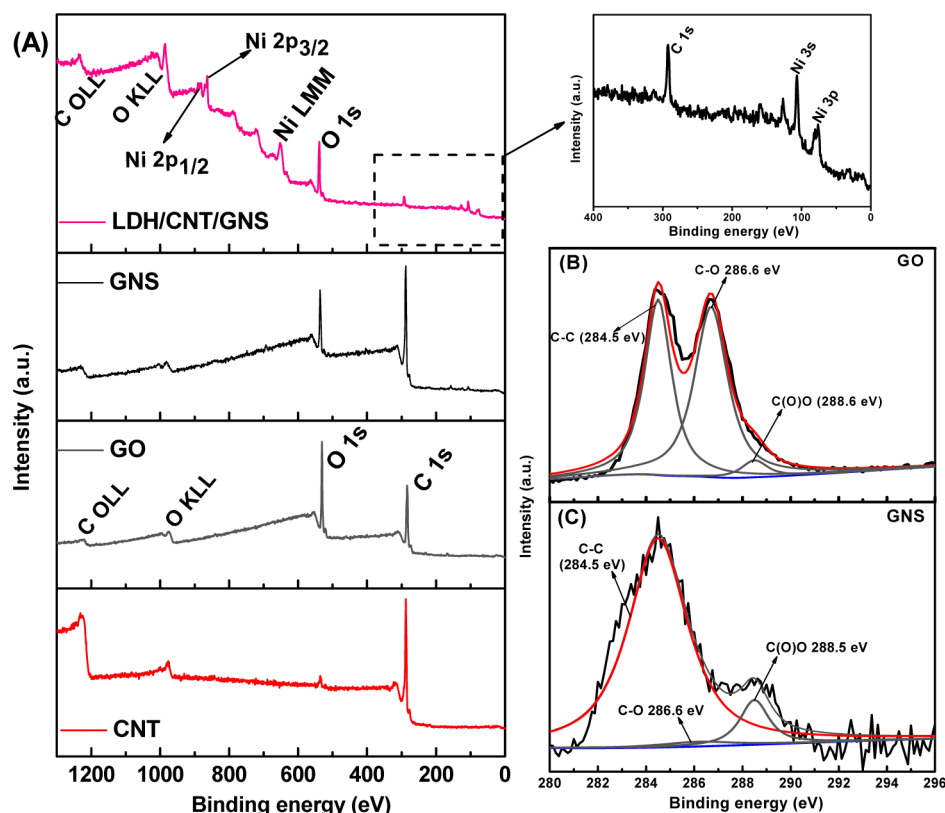


**Figure 5.** (A) XPS survey spectra of acid-treated CNT, GO, GNS, and LDH/CNT/GNS ternary composite; (B) C 1s spectra of GO and GNS.

for LDH/CNT sample, proving that multiwall carbon nanotubes are highly dispersed in hydrotalcite structure (Figure 4A e). And a small amount of CNTs imbedded into the LDHs did not impede the growth of LDH crystals. Furthermore, the XRD patterns of the samples added with GNSs (Figure 4A f, g) show a decrease intensity of (003) peak, corresponding to the lower crystallinity of the LDHs. And their obvious broadening diffraction peaks indicates smaller LDH particle sizes in LDH/GNS and LDH/CNT/GNS composites, which is consistent with the results of SEM images (Figures 2b and 3b). Moreover, no diffraction peaks from GNS are observed in Figure 4A f and g, indicating the totally exfoliation of GNS sheets in the composites. Previous research also shows that the diffraction peaks of GNS will become weak or even disappear, if the regular stacks of GO or graphite are greatly destroyed.<sup>46–48</sup>

The interactions of LDH platelets with CNTs and GNSs were also investigated by Raman spectroscopy, as shown in Figure 4B. For carbon materials CNT and GNS (Figure 4Ba, c), there are usually two feature peaks known as the D band and G band. The D band arises from a breathing mode of point photons of  $A_{1g}$  symmetry (usually observed at 1300–1400  $\text{cm}^{-1}$ ). The strength of D band relates to the quantity of disordered graphite and the conjugation degree disruption for GNS sheets. And the G band arises from the first order scattering of the  $E_{1g}$  phonon for  $\text{sp}^2$  C atoms (in the region of 1500–1600  $\text{cm}^{-1}$ ).<sup>49</sup> Compared with GNS, the Raman spectrum of acid-treated CNT has a larger intensity ratio of the D/G band ( $I_D/I_G$ ), implying the generation of oxygen-containing groups that introduced during the acid-treated process. This result is consistent with the absorption peaks of oxygen-containing groups in the FT-IR spectra and the O 1s peak in the XPS survey spectrum of CNT-COOH (Figures 4C and 5A). Two strong peaks located at 597 and 672  $\text{cm}^{-1}$  in

Figure 4B d are typically assigned to Ni–Al LDH.<sup>50</sup> Both the carbon peaks and the LDH peaks could be seen in all Raman spectrum of LDH-carbon composites, indicating the successful preparation of the composites.

The presence of oxygen-containing functional groups on CNTs, the reduction of GO and the formation of LDH-carbon composites were further investigated by FT-IR spectra (Figure 4C). Successful formation of hydroxyl and carboxylic groups on the side walls of CNTs after acid-treated process has been confirmed by –OH and –COOH stretching absorption peak (located at 3409 and 1546  $\text{cm}^{-1}$ ) in Figure 4C a. For GO (Figure 4C b), the characteristic features are the stretching vibration of C=O (carboxylic acid) at 1716  $\text{cm}^{-1}$  and C–O–H (alkoxy) at 1078  $\text{cm}^{-1}$ .<sup>51–54</sup> Two peaks at about 3420 and 1384  $\text{cm}^{-1}$  correspond to the stretching vibration and deformation vibration of O–H. The peak at 1622  $\text{cm}^{-1}$  originates from the vibrations of the adsorbed water molecules and the contributions from the skeletal vibrations of unoxidized graphitic domains.<sup>40,55</sup> For GNS (Figure 4Cc), the disappearance of C=O absorption peaks and the weaken of some peaks indicate the partial reduction of oxygen-containing groups on GO sheets. In the FT-IR spectra of LDH/CNT/GNS composite (Figure 4Cg), a broad absorption band around 3600–3200  $\text{cm}^{-1}$  centered at 3427  $\text{cm}^{-1}$  corresponds to the O–H stretching vibrations of hydroxyl groups of brucite layers and interlayer water molecules. The vibration of  $\text{CO}_3^{2-}$  at 1393, 1300, and 865  $\text{cm}^{-1}$  correspond to the interlayer anion of layered Ni–Al LDH, and the bands below 800  $\text{cm}^{-1}$  are ascribed to metal–oxygen (M–O) stretching, which are consistent with the previous reports.<sup>50,56</sup>

Further chemical composition information on the surface of GO, CNT, GNSs and LDH/CNT/GNS composite was analyzed by XPS spectrum. As shown in Figure 5A, the

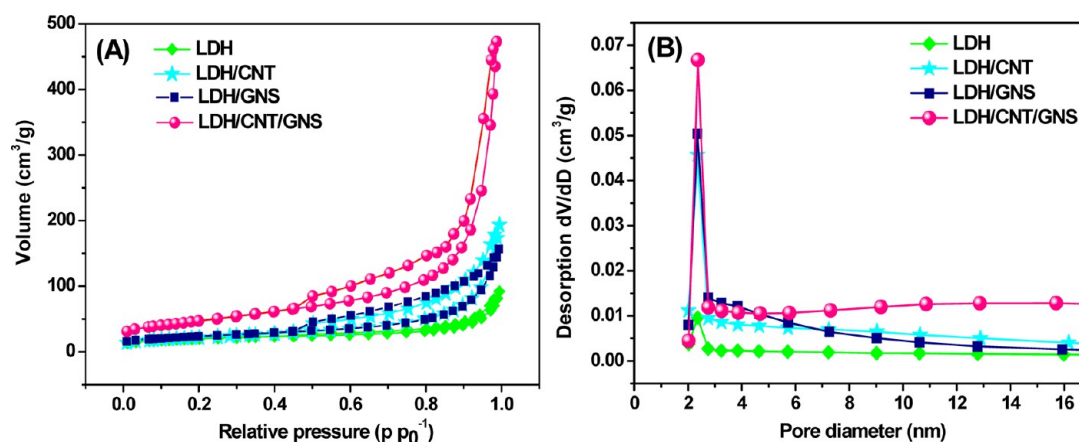
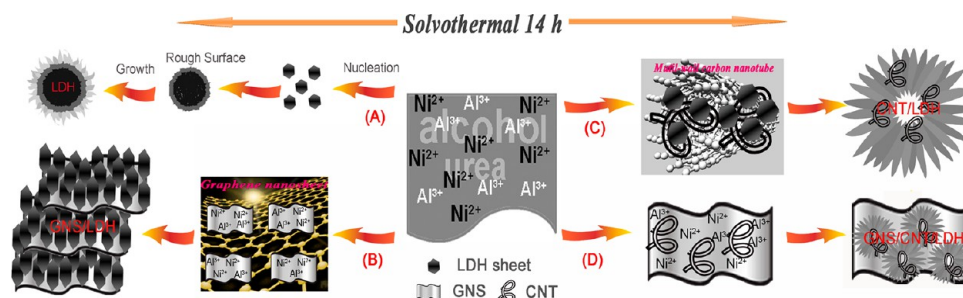


Figure 6. (A)  $N_2$  adsorption/desorption isotherm and (B) pore size distribution of pristine Ni–Al LDH and LDH–carbon composites.

Scheme 1. Schematic Representation of the Possible Self-Assembly Process of Pure Ni–Al LDH Microspheres, LDH/CNT, LDH/GNS, and LDH/CNT/GNS Composites



appearance of a series of Ni vibration peaks in the XPS spectrum for LDH/CNT/GNS, compared to that of CNT and GNS, clearly indicates the introduction of LDH platelets into GNS sheets and CNTs. The C1s spectrum of GO and GNS can be decomposed into three components: (1) the aromatic linked carbon ( $\text{C}=\text{C}$ , 284.8 eV), (2) the C in oxygen single-bonded carbon bonds ( $\text{C}-\text{O}$ , 286.2 eV), (3) the carboxylate carbon ( $\text{O}-\text{C}=\text{O}$ , 289.0 eV).<sup>57</sup> As seen from Figure 5B, GO shows a main peak at 284.6 eV, which could be ascribed to the component of  $\text{C}=\text{C}$ . Another two strong peaks could be observed at 286.1 and 288.1 eV, which suggests considerable oxidation degree in the graphite plane. Compared with GO, the signal of  $\text{C}-\text{O}$  and  $\text{O}-\text{C}=\text{O}$  in C 1s spectrum of the GNS (Figure 5C) becomes much weaker. By integrating the area of these peaks,<sup>58</sup> the percentage of nonoxygenated ring C was calculated to be 33.6% for GO, and 65% for GNS sample after treatment with glucose. These results imply that considerable deoxygenation occurred by glucose reduction resulting in the recovery of the conductivity of GO, whereas a small amount of residual oxygen-containing groups still exist on GNS sheets becoming the anchor sites for in situ growth of LDH crystals.

The electrode materials need the specific surface areas as higher as possible to accommodate more and more superficial electrochemical active sites to participate in the Faradaic redox reactions. And suitable mesopores of electrode materials (especially pores at about 2–5 nm) are also critical to reduce the mass transfer of electrolytes in fast Faradaic redox reactions. Therefore, the products were further investigated by  $N_2$ -adsorption/desorption measurement for their surface area and porosity property (Figure 6). In the case of LDH/GNS and LDH/CNT/GNS (Figure 6A), there appeared a typical IV isotherm with  $H_3$ -type hysteresis loops ( $P/P_0 > 0.4$ ), which

indicates the presence of mesopores.<sup>59</sup> Any limiting adsorption at high  $P/P_0$  region is not exhibited for this type of hysteresis loops, which is usually ascribed to the particle aggregates with slit-shaped pores.<sup>60</sup> And larger Brunauer–Emmet–Teller (BET) surface areas are observed for both LDH/GNS (62.1  $\text{m}^2/\text{g}$ ) and LDH/CNT/GNS (169.1  $\text{m}^2/\text{g}$ ) composites, compared with that of LDH/CNT (53.9  $\text{m}^2/\text{g}$ ) composite and LDH microspheres (24.1  $\text{m}^2/\text{g}$ ). It is reasonable to believe that the introduction of GNS in the composite reduces the aggregation of LDH platelets, thus leading to more surfaces of LDH exposed to the electrolyte. On the other hand, large amounts of LDH platelets or LDH/CNT spheres in situ uniformly dispersed onto GNS matrixes in the LDH/CNT/GNS composite, which effectively separate the GNS sheets, leading to the narrow pore size distributions and higher surface areas. In Figure 6B, the pore size shows a narrow distribution in the range below 20 nm for all the samples, and the average pore radius are in the size of 2–3 nm. It is noted that the total pore volume of LDH/CNT/GNS sample is larger than those of other samples, which are mainly resulted from the interstitial space between LDHs, CNTs, and GNS sheets. From the above results, we believe that the GNS here was exfoliated by the LDH/CNT nanoflowers and the GNS with theoretically high specific surface area improves the utility of Ni–Al LDHs simultaneously.

**3.2. Formation Mechanism for 3D LDH/CNT/GNS Composite.** On the basis of the above analysis, the formation process for the pristine LDH and the LDH–carbon composites is schematically illustrated in Scheme 1. As our previous report, the Ni–Al LDH and LDH-based composites are formed in a solvothermal system, which has a similar formation mechanism.<sup>34</sup> Briefly, ethanol was used as the solvent due to its high



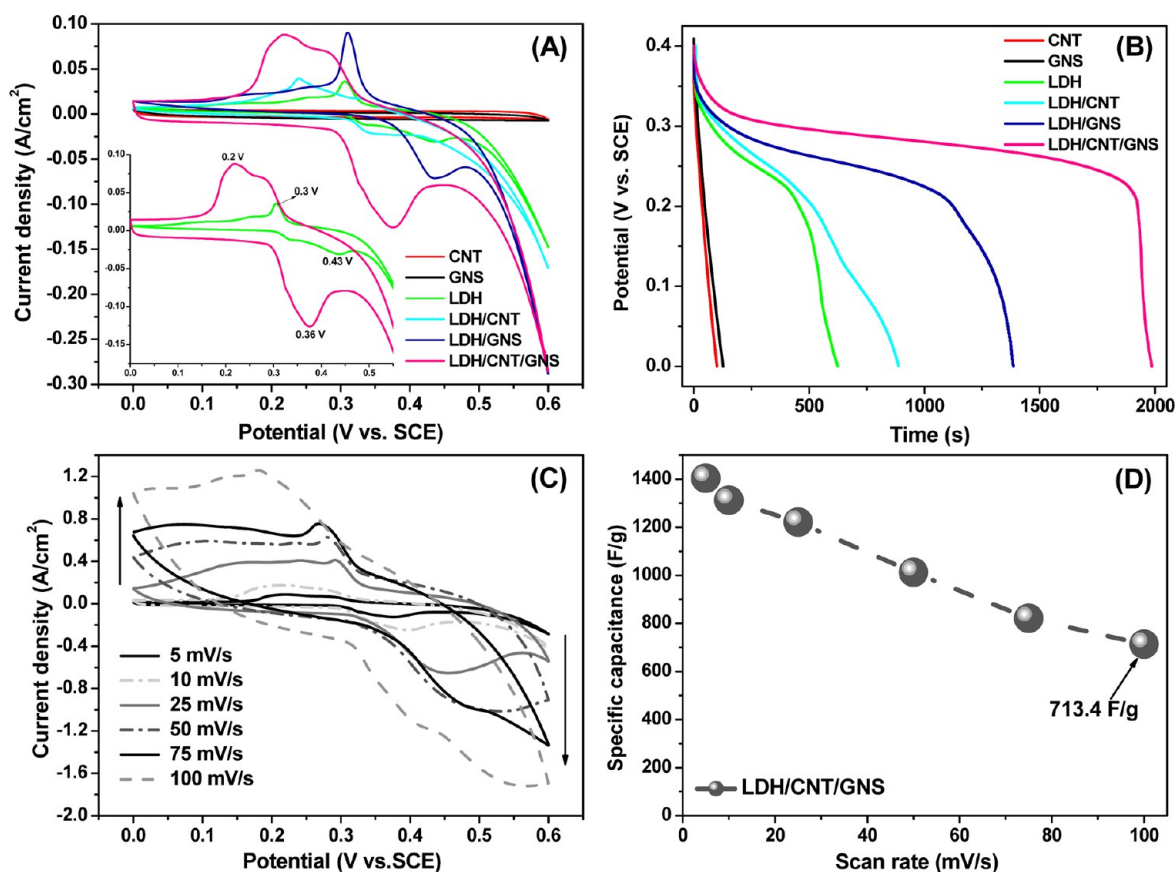


**Figure 7.** (A) CV curves of all samples at the scan rate of 10 mV/s in 6 M KOH solution; (B) discharge curves of all samples measured at the constant discharge density of 5 mA/cm<sup>2</sup>; (C) CV curves of LDH/CNT/GNS composite at different scan rates of 5, 10, 25, 50, 75, and 100 mV/s; (D) specific capacitance of LDH/CNT/GNS electrode at different scan rates that calculated from CV curves.

boiling point and relative strong polarity, and its coordinated ability. These properties have an influence on the polarity and the solubility of reactants during the preparation, which will change surface energy and reduce the crystal growth rate, leading to the formation of the unique structure. For pristine Ni–Al LDH, because of the high lateral growth rate along a direction, the LDH platelet exhibits a hexagonal morphology in the initial coprecipitation. Then these hexagonal sheets further randomly accumulate to irregular aggregates. During the reaction process, the reactants concentration decreased in the reaction system and finally established a chemical equilibrium between the solid–liquid interfaces. At the same time, there is a nonequilibrium state in the interior smaller crystallites. In the course of crystallization, the exterior crystallites serve as nucleation points to attract the smaller metastable crystallites underneath the outer surface layer. Through this process, LDH crystallites gradually assembled into hexagonal structure. This structural formation mechanism of nanocrystallites is called “oriented attachment”, the formed crystallites could further fuse together with their high-energy surfaces under crystallographic fusion.<sup>61</sup> Finally, the uniform mesoporous structure formed between LDH platelets on the surface of initial aggregates.

In this paper, nitric acid oxidation was applied for functionalization of pristine CNTs, which not only improves its water-soluble, but also induces its surface with oxygen-containing functional groups. As the residual oxygen-containing groups on GNS sheets, they could act as nucleation sites for the in situ formation of LDH nanostructures. For LDH/GNS

composite, Ni<sup>2+</sup> and Al<sup>3+</sup> in solution could first form coordination complexes with carboxyl and hydroxyl groups of GNSs through the electrostatic attraction. After addition of urea, Ni<sup>2+</sup> and Al<sup>3+</sup> ions will coprecipitate and form the LDH crystal nucleus on the coordination sites (as shown in eq 1), which provides the necessary heterogeneous nucleation sites. Then, the formed positively charged lattices of LDH crystals attached to the negatively charged carboxylic groups on the surfaces of GNS, and finally grew up to LDH nanosheets. Finally, a large amount of LDH platelets grew vertically onto the GNS matrix, greatly improved the utility of the two components. When the acid-treated CNT was added to the reaction system, the spherical morphology of LDH/CNT particles with LDH platelets and CNTs interleaved together, which indicated a same growth process as the flowerlike LDH/CNT binary composite. In addition to the connection of LDHs with carboxyl groups on CNTs, the electrostatic force also exists between LDHs and GNS sheets, which could be demonstrated by the strong ultrasonic vibration during the preparation process of TEM sample. Furthermore, the CNTs could be used as spacers to hinder the agglomeration of LDH platelets, making full use of the internal structure of LDH particles. In LDH/CNT/GNS ternary composite, strong electrostatic interaction between LDH platelets and carbons may take place to lead to form a special 3D superstructure and maximize the BET surface area and porosity that are the two most important factors influencing the properties of electrode materials. So, such open structure of the ternary nanocomposite

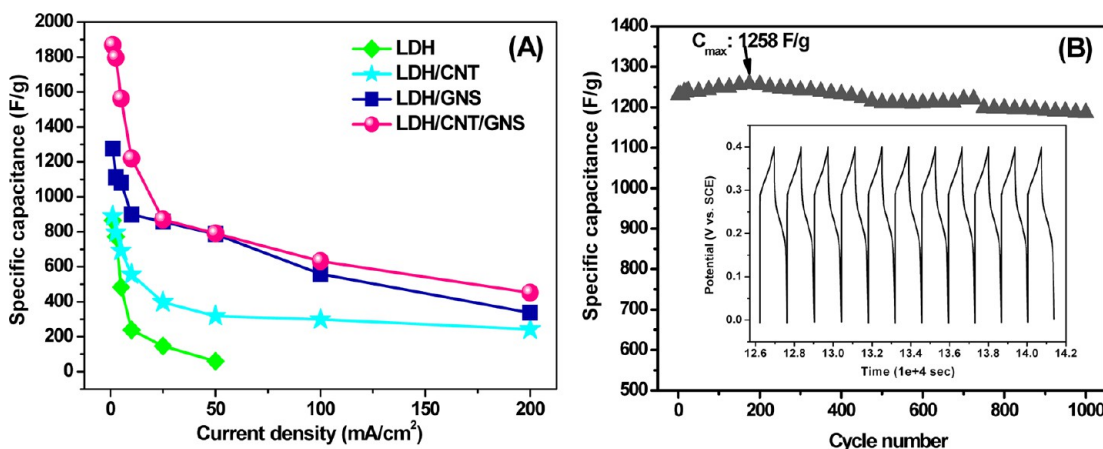
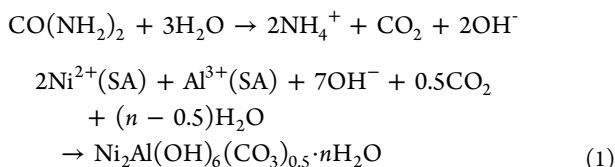


**Figure 8.** (A) Specific capacitances of Ni–Al LDH, LDH/CNT, LDH/GNS, and LDH/CNT/GNS composites at different current densities; (B) cycle performance of LDH/CNT/GNS electrode at the current density of 10 mA/cm<sup>2</sup> (inset is the galvanostatic charge/discharge curves).

may be favorable for the improvement of the electrochemical performance for SCs.



**3.3. Electrochemical Performance.** For the highly open framework of LDH/CNT/GNS nanostructure, which is the ideal morphological foundation for fast redox reaction and charge accumulation, its potential application in high-performance supercapacitor has been investigated by cyclic voltammetry (CV), galvanostatic charge–discharge and electrochemical impedance (EIS) measurements in 6 M KOH solution. Figure 7A illustrates the CV curves for all the products at the scan rate of 10 mV/s. The profiles of the CV curves for CNT and GNS are relatively flat and rectangular, which is typical for EDLCs.<sup>62</sup> For pristine Ni–Al LDH, a pair of redox peaks (anodic peak at around 0.3 V and cathodic peak at about 0.43 V) are observed, which corresponds to the transition between the different oxidation states of Ni according to the eq 2<sup>63</sup>



The CV curves of other LDH–carbon composites also exhibit the similar redox peaks with varying degrees of deviation, which is due to the impact of the different carbon sources on the electrochemical behavior of LDH. Furthermore, the current density response and CV integral areas of LDH–carbon electrodes are much larger than that of pristine LDH, corresponding higher specific capacitance of the composites. Figure 7B compares the discharge curves of all the samples at the current densities of 5 mA/cm<sup>2</sup>. Two obvious different sections appeared in the discharge curve, a fast potential drop followed by a slow potential decay. The first potential drop attributed to the internal resistance of the electrode, and the subsequent potential decay represented the capacitive feature of the pseudocapacitive electrode. The specific capacitance (*C*) of LDH/CNT, LDH/GNS and LDH/CNT/GNS electrodes obtained from the discharge time is measured to be 691.4, 1081, and 1562 F/g, respectively (eq 3). The higher capacitance of LDH/GNS than that of LDH/CNT is ascribed to the special structure LDH/GNS with LDH nanosheets

vertical growing on the surface of conductive GNS. The capacitance of LDH/CNT/GNS is more than three times larger than that of pristine LDH (484 F/g), which is mainly due to its enhanced electrical conductivity and specific surface area. CV curves of LDH/CNT/GNS electrode at different scan rates are shown in Figure 7C. The potential difference ( $\Delta E_{a,c}$ ) between the anodic and cathodic peaks is used to measure the reversibility of the electrochemical redox reaction.<sup>64</sup> Each curve at the different scan rates kept similar redox couples, which indicates that quasi-reversible and continuous Faradic redox reactions of Ni–Al LDH are involved during the charge and discharge processes contributing the pseudocapacitance to the total capacitance. Specific capacitance of the LDH/CNT/GNS electrode at different scan rates calculated from CVs through eq 4 is presented in Figure 7D. With the increase of scan rates, the value of capacitance gradually decreased. At high scan rates, the movement of ions and protons are most likely limited by the diffusion, and only the outer active surface could be utilized for charge storage, leading to low electrochemical utilization of electroactive materials.<sup>65</sup> The maximum specific capacitance for the ternary composite reaches 1404 F/g at 5 mV/s, and maintain at 713.4 F/g when the scan rate is up to 100 mV/s, indicating an excellent current corresponding performance of the LDH/CNT/GNS electrode. The specific capacitance (*C*) can be calculated by the following equation

$$C = \frac{A}{Vm\Delta V} \quad (3)$$

$$C = \frac{It}{\Delta Vm} \quad (4)$$

in which *A* is the integral area of CV curves, *V* is the scan rate (V/s), *m* is the mass of active materials (g),  $\Delta V$  is the potential window of discharge (V), *I* is the constant current (A), and *t* is the discharge time (s), respectively.

Good rate performance and long cycling life are important requirements for SCs. Figure 8A shows the specific capacitance of pure Ni–Al LDH and LDH–carbon composites at the different current density. Among them, LDH/CNT/GNS composite with highly open nanostructure shows the highest capacitance and the best rate performance. The enhancement of capacitance is mainly attributed to the effective utilization of Ni ions due to the mesoporous structures and the large surface area for charge-transfer reactions. Moreover, the decrease in

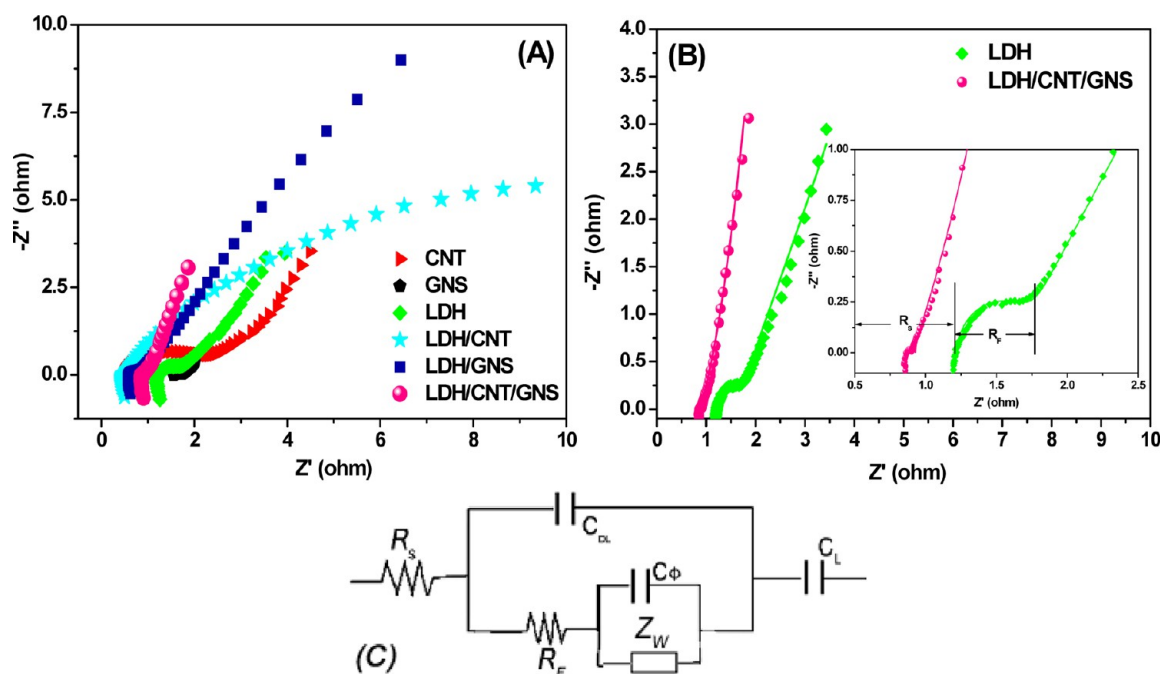


**Figure 9.** (A) Nyquist plots of experimental impedance (EIS) of all samples in the frequency range of 100 kHz to 0.05 Hz; (B) EIS data (scattering dot) and fitting results (solid line) for pure Ni–Al LDH and LDH/CNT/GNS electrodes; (C) electrical equivalent circuit used for fitting impedance spectra for LDH and LDH/CNT/GNS composite.

**Table 1.** Calculated Values of  $R_s$ ,  $C_{DL}$ ,  $R_F$ ,  $C_\phi$ ,  $Z_W$ , and  $C_L$  through CNLS Fitting of the Experimental Impedance Spectra Based on the Proposed Equivalent Circuit in Figure 9B

	$R_s$ ( $\Omega$ )	$C_{DL}$ (F)	$R_F$ ( $\Omega$ )	$C_\phi$ (F)	$Z_W$ ( $\Omega$ )	$C_L$ (F)
LDH	1.268	0.002598	0.5219	0.02155	0.1832	0.6016
LDH/CNT/GNS	0.92	0.2588	0.02254	0.0002237	1.192	1.39

capacitance at high current densities is due to the inner inaccessible active sites that are unable to completely sustain the redox transitions. The specific capacitance of LDH/CNT/GNS electrode was calculated to be 1869, 1796, and 1562 F/g based on the total mass of the composite, respectively, corresponding to discharge current densities of 1, 2.5, and 5 mA cm<sup>-2</sup> (Figure 8C), which are much larger than that of the previous works on LDH-based composite electrode material. The improved rate performance of the LDH/CNT/GNS composite can be ascribed to the addition of the CNTs makes the LDH nanosheets assemble to the much smaller LDH/CNT sphere, which finally contributes to form more open loose structure. Besides, Figure 8B shows the cyclic performances of the LDH/CNT/GNS electrode examined by galvanostatic charge–discharge tests for 1000 cycles. At the current density of 10 mA/cm<sup>2</sup>, the LDH/CNT/GNS electrode exhibited excellent electrochemical stability with only 3.5% deterioration of the initial available capacitance after 1000 cycles. Interestingly, the specific capacitance of LDH/CNT/GNS electrode increases by 22.8% after 175 cycle tests. This may be ascribed to the active materials could not be fully used at the initial stage. With the increase of cyclic numbers, the electrochemical active sites inside the electrode materials may be fully exposed to the electrolyte, more electrochemical active LDH takes part in the redox reaction. Therefore, a maximum capacitance of 1258 F/g is displayed. The better cycling stability and longer lifetime of LDH/CNT/GNS composite compared to traditional Ni–Al LDHs is result from the

introduction of CNTs and GNSs with high mechanical property and conductivity.

An electrochemical impedance technique (EIS) was employed to better understand the difference of electrochemical behavior for LDH/CNT/GNS nanocomposite and other components. The EIS data were analyzed by Nyquist plots as shown in Figure 9A. All of the EIS plots of these samples contained a partially overlapped semicircle and a straight sloping line. Obviously, the semicircle in the high frequency range of all the LDH-carbon composites is smaller than that of pristine LDH sample, corresponding to a smaller charge transfer resistance ( $R_F$ ) caused by the redox reactions and the double-layer capacitance ( $C_{DL}$ ) on the surfaces of electrode materials. At the low frequencies, the impedance plot theoretically should be a vertical line, which is parallel to the imaginary axis. The straight line of LDH/CNT/GNS electrode close to 90° indicated a pure capacitive behavior and a low diffusion resistance of ions in the structure of this ternary composite. The measured impedance spectra of LDH and LDH/CNT/GNS were further analyzed by the complex nonlinear least-squares (CNLS) fitting method based on the equivalent circuit, which is given in the Figure 9C. The fitting results are presented in Table 1, where the  $R_s$  is bulk resistance of the electrochemical system (the intersection of the curve at real part  $Z'$  in the high frequencies range),  $Z_W$  is the Warburg impedance (the slope of the curves at a low frequency). Among all the evaluation parameters, the  $R_s$  and  $R_F$  of LDH/CNT/GNS composite are clearly smaller than that of pristine LDH,



which demonstrates that the addition of CNTs and GNSs enhances the conductivity of the composites.

#### 4. CONCLUSION

In this paper, a simple ethanol solvothermal method was developed to prepare Ni–Al LDH/CNT/GNS composite. As described by the above various characterizations, flowerlike LDH/CNT particles coated on the surfaces of GNS sheets to generate a 3D hybrid material that homogeneously coexist at a nanometer level. The LDH/CNT/GNS hybrid electrode exhibited ultrahigh specific capacitance, good rate performance, and long cycle-life in the electrochemical tests. The overall improvement of the electrochemical performances of LDH/CNT/GNS electrode is mainly due to the following three factors: (1) Addition of carbon materials into LDH produces a synergic effect with GNS used as conductive substrate and CNTs in the LDH/CNT sphere as electron transmission channel resulting in low internal electrical resistance for efficient charge transport in the hybrid electrode; (2) The interconnected Ni–Al LDH platelets of the flowerlike LDH/CNT nanostructure create many mesopores, which benefits electrolyte transport and shortens the ions diffusion paths in the inner of the active materials; (3) The porous open nanostructure of LDH/CNT/GNS composite with high specific surface area hinders the agglomeration of the individual components, and effectively improves their utilization. Overall, the LDH/CNT/GNS ternary nanocomposite could be promising for fabrication of high-performance supercapacitors. And the findings in this work are also meaningful for understanding the self-assembly process of LDH and may provide a direction for the synthesis of other GNS/CNT-based ternary composite materials.

#### AUTHOR INFORMATION

##### Corresponding Author

\*E-mail: zhqw1888@sohu.com. Tel.: +86 451 8253 3026. Fax: +86 451 8253 3026.

##### Notes

The authors declare no competing financial interest.

#### ACKNOWLEDGMENTS

This work was supported by Special Innovation Talents of Harbin Science and Technology (2011RFQXG016), Fundamental Research Funds of the Central University (HEUCFZ), Key Program of the Natural Science Foundation of Heilongjiang Province (ZD201219), Program of International S&T Cooperation special project (2013DFA50480), Special Innovation Talents of Harbin Science and Technology (2012RFXXG104).

#### REFERENCES

- (1) Conway, B. E. *J. Electrochem. Soc.* **1991**, *138*, 1539–1548.
- (2) Frackowiak, E.; Béguin, F. *Carbon* **2001**, *39*, 937–950.
- (3) Simon, P.; Gogotsi, Y. *Nat. Mater.* **2008**, *7*, 845–854.
- (4) Liu, C.; Li, F.; Ma, L. P.; Cheng, H. M. *Adv. Mater.* **2010**, *22*, E28–E62.
- (5) Adhyapak, P. V.; Maddanimath, T.; Pethkar, S. A.; Chandwadkar, J.; Negi, Y. S.; Vijayamohanan, K. *J. Power Sources* **2002**, *109*, 105–110.
- (6) Novoselov, K. S.; Geim, A. K.; Morozov, S. V.; Jiang, D.; Zhang, Y.; Dubonos, S. V.; Grigorieva, I. V.; Firsov, A. A. *Science* **2004**, *306*, 666–669.
- (7) Yang, W.; Ratnac, K. R.; Ringer, S. P.; Thordarson, P.; Gooding, J. J.; Braet, F. *Angew. Chem., Int. Ed.* **2010**, *49*, 2114–2138.
- (8) Baughman, R. H.; Zakhidov, A. A.; de Heer, W. A. *Science* **2002**, *297*, 787–792.
- (9) Choi, B. G.; Chang, S. J.; Kang, H. W.; Park, C. P.; Kim, H. J.; Hong, W. H.; Lee, S.; Huh, Y. S. *Nanoscale* **2012**, *4*, 4983–4988.
- (10) Yang, W.; Gao, Z.; Wang, J.; Wang, B.; Liu, Q.; Li, Z.; Mann, T.; Yang, P.; Zhang, M.; Liu, L. *Electrochim. Acta* **2012**, *69*, 112–119.
- (11) Wang, J.; Gao, Z.; Li, Z.; Wang, B.; Yan, Y.; Liu, Q.; Mann, T.; Zhang, M.; Jiang, Z. *J. Solid State Chem.* **2011**, *184*, 1421–1427.
- (12) Tien, H. W.; Huang, Y. L.; Yang, S. Y.; Hsiao, S. T.; Wang, J. Y.; Ma, C. C. M. *J. Mater. Chem.* **2011**, *21*, 14876–14883.
- (13) Yu, D.; Dai, L. *J. Phys. Chem. Lett.* **2010**, *1*, 467–470.
- (14) Wang, Y.; Wu, Y.; Huang, Y.; Zhang, F.; Yang, X.; Ma, Y.; Chen, Y. *J. Phys. Chem. C* **2011**, *115*, 23192–23197.
- (15) Chen, S. Q.; Chen, P.; Wang, Y. *Nanoscale* **2011**, *3*, 4323–4329.
- (16) Cai, D.; Song, M.; Xu, C. *Adv. Mater.* **2008**, *20*, 1706–1709.
- (17) Yung, V. C.; Chen, L.; Allen, M. J.; Wassei, J. K.; Nelson, K.; Kaner, R. B.; Yang, Y. *Nano Lett.* **2009**, *9*, 1949–1955.
- (18) Lei, Z.; Shi, F.; Lu, L. *ACS Appl. Mater. Interfaces* **2012**, *4*, 1058–1064.
- (19) Rives, V. *Layered Double Hydroxides: Present and Future*; Nova Science Publishers: New York, 2001.
- (20) Wang, J.; Zhou, J.; Li, Z.; Liu, Q.; Yang, P.; Jing, X.; Zhang, M. *Mater. Res. Bull.* **2010**, *45*, 640–645.
- (21) Wang, Q.; O'Hare, D. *Chem. Rev.* **2012**, *112*, 4124–4155.
- (22) Del Hoyo, C. *Appl. Clay Science* **2007**, *36*, 103–109.
- (23) Evans, D. G.; Duan, X. *Chem. Commun.* **2006**, *6*, 485–496.
- (24) Williams, G. R.; O'Hare, D. *J. Mater. Chem.* **2006**, *16*, 3065–3074.
- (25) Liu, X. M.; Zhang, Y. H.; Zhang, X. G.; Fu, S. Y. *Electrochim. Acta* **2004**, *49*, 3137–3141.
- (26) Malak-Polaczyk, A.; Vix-Guterl, C.; Frackowiak, E. *Energy Fuels* **2010**, *24*, 3346–3351.
- (27) Wang, L.; Wang, D.; Dong, X. Y.; Zhang, Z. J.; Pei, X. F.; Chen, X. J.; Chen, B.; Jin, J. *Chem. Commun.* **2011**, *47*, 3556–3558.
- (28) Su, L. H.; Zhang, X. G.; Yang, L. *J. Solid State Electrochem.* **2008**, *12*, 1129–1134.
- (29) Géraud, E.; Rafqah, S.; Sarakha, M.; Forano, C.; Prevot, V.; Leroux, F. *Chem. Mater.* **2007**, *20*, 1116.
- (30) Stimpfling, T.; Leroux, F. *Chem. Mater.* **2010**, *22*, 974–987.
- (31) Gao, Z.; Wang, J.; Li, Z.; Yang, W.; Wang, B.; Hou, M.; He, Y.; Liu, Q.; Mann, T.; Yang, P.; Zhang, M.; Liu, L. *Chem. Mater.* **2011**, *23*, 3509–3516.
- (32) Dong, X.; Wang, L.; Wang, D.; Li, C.; Jin, J. *Langmuir* **2011**, *28*, 293–298.
- (33) Chen, D.; Wang, X.; Liu, T.; Wang, X.; Li, J. *ACS Appl. Mater. Interfaces* **2010**, *2*, 2005–2011.
- (34) Song, Y.; Wang, J.; Li, Z.; Guan, D.; Manna, T.; Liu, Q.; Zhang, M.; Liu, L. *Microporous Mesoporous Mater.* **2012**, *148*, 159–165.
- (35) Zhu, C.; Guo, S.; Fang, Y.; Dong, S. *ACS Nano* **2010**, *4*, 2429–2437.
- (36) Hummers, W. S.; Offeman, R. E. *J. Am. Chem. Soc.* **1958**, *80*, 1339–1339.
- (37) Zhao, X.; Wang, A.; Yan, J.; Sun, G.; Sun, L.; Zhang, T. *Chem. Mater.* **2010**, *22*, 5463–5473.
- (38) Zhang, L.; Zhang, X.; Shen, L.; Gao, B.; Hao, L.; Lu, X.; Zhang, F.; Ding, B.; Yuan, C. *J. Power Sources* **2012**, *199*, 395–401.
- (39) Kuang, Y.; Zhao, L.; Zhang, S.; Zhang, F.; Dong, M.; Xu, S. *Materials* **2010**, *3*, 5220–5235.
- (40) Sun, Z.; Liu, Z.; Han, B.; Wang, Y.; Du, J.; Xie, Z.; Han, G. *Adv. Mater.* **2005**, *17*, 928–932.
- (41) Liu, Z. H.; Wang, Z. M.; Yang, X.; Ooi, K. *Langmuir* **2012**, *18*, 4926–4930.
- (42) Hassan, H. M. A.; Abdelsayed, V.; Khder, A. E. R. S.; Zeid, K. M.; Ternier, J.; Shall, M. S.; Resayes, S. I.; Azhary, A. A. *J. Mater. Chem.* **2009**, *19*, 3832–3837.
- (43) McAllister, M. J.; Li, J. L.; Adamson, D. H.; Schniepp, H. C.; Abdala, A. A.; Liu, J.; Alonso, M. H.; Milius, D. L.; Car, R.; Prud'homme, R. K.; Aksay, I. A. *Chem. Mater.* **2007**, *19*, 4396–4404.
- (44) Su, L. H.; Zhang, X. G. *J. Power Sources* **2007**, *172*, 999–1006.

- (45) Miyaya, S. *Clays Clay Miner.* **1983**, *31*, 305–311.
- (46) Nethravathi, C.; Nisha, T.; Ravishankar, N.; Shivakumara, C.; Rajamathi, M. *Carbon* **2009**, *47*, 2054–2059.
- (47) Lambert, T. N.; Chavez, C. A.; Sanchez, B. H.; Lu, P.; Bell, N. S.; Ambrosini, A.; Friedman, T.; Boyle, T. J.; Wheeler, D. R.; Huber, D. L. *J. Phys. Chem. C* **2009**, *113*, 19812–19823.
- (48) Xu, C.; Wu, X.; Zhu, J.; Wang, X. *Carbon* **2008**, *46*, 386–389.
- (49) Wang, G.; Yang, J.; Park, J.; Guo, X.; Wang, B.; Liu, H.; Yao, J. *J. Phys. Chem. C* **2008**, *112*, 8192–8195.
- (50) Liu, Z.; Ma, R.; Osada, M.; Lyi, N.; Ebina, Y.; Takada, K.; Sasaki, T. *J. Am. Chem. Soc.* **2006**, *128*, 4872–4880.
- (51) O'Connell, M. J.; Bachilo, S. M.; Huffman, C. B.; Moore, V. C.; Strano, M. S.; Haroz, E. H.; Rialon, K. L.; Boul, P. J.; Noon, W. H.; Kittrell, C.; Ma, J.; Hauge, R. H.; Weisman, R. B.; Smalley, R. E. *Science* **2002**, *297*, 593–596.
- (52) Richard, C.; Balavoine, F.; Schultz, P.; Ebbesen, T. W.; Mioskowski, C. *Science* **2003**, *300*, 775–778.
- (53) Dieckmann, G. R.; Dalton, A. B.; Johnson, P. A.; Razal, J.; Chen, J.; Giordano, G. M.; Munoz, E.; Musselman, I. H.; Baughman, R. H.; Draper, R. K. *J. Am. Chem. Soc.* **2003**, *125*, 1770–1777.
- (54) Zheng, M.; Jagota, A.; Semke, E. D.; Diner, B. A.; McLean, R. S.; Lustig, S. R.; Richardson, R. E.; Tassi, N. G. *Nat. Mater.* **2003**, *2*, 338–342.
- (55) Xu, Y.; Bai, H.; Lu, G.; Li, C.; Shi, G. *J. Am. Chem. Soc.* **2008**, *130*, 5856–5857.
- (56) Guo, S.; Zhang, C.; Peng, H.; Wang, W.; Liu, T. *Compos. Sci. Technol.* **2011**, *71*, 791–796.
- (57) Yang, D.; Velamakanni, A.; Bozoklu, G.; Park, S.; Stoller, M.; Piner, R. D.; Stankovich, S.; Jung, I.; Field, D. A.; Ventrice, C. A., Jr.; Ruoff, R. S. *Carbon* **2009**, *47*, 145–152.
- (58) Wang, L.; Wang, D.; Dong, X. Y.; Zhang, Z. J.; Pei, X. F.; Chen, X. J.; Chen, B.; Jin, J. *Chem. Commun.* **2011**, *47*, 3556–3558.
- (59) Yu, J.; Yu, J. C.; Ho, W.; Leung, M. K.P.; Cheng, B.; Zhang, G.; Zhao, X. *Appl. Catal. A: General* **2003**, *255*, 309–320.
- (60) Sing, K. S. W.; Everett, D. H.; Haul, R.A. W.; Moscou, L.; Pierotti, R. A.; Rouquerol, J.; Siemieniowska, T. *Pure Appl. Chem.* **1985**, *57*, 603–619.
- (61) Zhong, L.; Hu, J.; Liang, H.; Cao, A.; Song, W.; Wan, A. *Adv. Mater.* **2006**, *18*, 2426–2431.
- (62) Li, H. Q.; Liu, R. L.; Zhao, D. Y.; Xia, Y. Y. *Carbon* **2007**, *45*, 2628–2635.
- (63) Xu, M. W.; Bao, S. J.; Li, H. L. *J. Solid State Electrochem.* **2007**, *11*, 372–377.
- (64) Zhu, W. H.; Ke, J. J.; Yu, H. M.; Zhang, D. J. *J. Power Sources* **1995**, *56*, 75–79.
- (65) Lao, Z. J.; Konstantinov, K.; Tournaire, Y.; Ng, S. H.; Wang, G. X.; Liu, H. K. *J. Power Sources* **2006**, *162*, 1451–1454.